

## Solidarity of signal of measures for the liquid-gas phase transition in the statistical multifragmentation model

W. Lin (林炜平),<sup>1</sup> P. Ren (任培培),<sup>1</sup> H. Zheng (郑华),<sup>2,\*</sup> X. Liu (刘星泉),<sup>1,3,†</sup> M. Huang (黄美容),<sup>4</sup>  
K. Yang (杨昆),<sup>5</sup> G. Qu (曲国峰),<sup>1</sup> and R. Wada<sup>6</sup>

<sup>1</sup>Key Laboratory of Radiation Physics and Technology of the Ministry of Education, Institute of Nuclear Science and Technology, Sichuan University, Chengdu 610064, China

<sup>2</sup>School of Physics and Information Technology, Shaanxi Normal University, Xi'an 710119, China

<sup>3</sup>Institute of Modern Physics, Chinese Academy of Sciences, Lanzhou, 730000, China

<sup>4</sup>College of Physics and Electronics information, Inner Mongolia University for Nationalities, Tongliao, 028000, China

<sup>5</sup>School of Physics and Engineering Technology, Xingyi Normal University for Nationalities, Xingyi 562400, China

<sup>6</sup>Cyclotron Institute, Texas A&M University, College Station, Texas 77843, USA



(Received 10 October 2018; revised manuscript received 25 January 2019; published 15 May 2019)

A systematic study of system size,  $N/Z$  asymmetry, and fragmenting volume effects as well as the Coulomb effect on experimental measures for the nuclear liquid-gas phase transition and the mechanism of phase transition are carried out in the framework of the statistical multifragmentation model (SMM). The measures examined here are the caloric curve, the specific heat capacity ( $C_v$ ), the multiplicity derivative ( $dM/dT$ ), the moment parameters ( $M_2$  and  $\gamma_2$ ), the fluctuation of maximum fragment charge number (NVZ), the Fisher exponent ( $\tau$ ), and the Zipf's law parameter ( $\xi$ ). A signal for the first-order phase transition for all the measures is observed. A stronger signal is observed in the system with smaller sizes or with more neutron rich or in smaller fragmenting volumes for the caloric curve,  $C_v$ , and  $dM/dT$ . The phase-transition temperatures are independent of the system size,  $N/Z$  asymmetry, fragmenting volume, and Coulomb force, which indicates these measures give a solid signal for the liquid-gas phase transition in SMM. On the other hand, the phase transition temperature and its behavior of the others slightly depend on the size, the  $N/Z$  asymmetry and the volume of the system. A negative heat capacity is observed for systems with  $A_s \geq 100$  without the Coulomb force but disappears with the Coulomb. An instructive picture is given in the charge distributions for the observed first-order phase transition.

DOI: [10.1103/PhysRevC.99.054616](https://doi.org/10.1103/PhysRevC.99.054616)

### I. INTRODUCTION

The nuclear multifragmentation process, which was predicted long ago [1] and has been extensively studied following the advent of  $4\pi$  detectors [2–4], provides a wealth of information on nuclear dynamics, on the properties of the nuclear equation of state and on the possible nuclear liquid-gas phase transition. The nuclear liquid-gas phase transition was first suggested in the early 1980s [5–7] and has been suggested for the observations in experimental results and theoretical simulations, because of the resemblance between the equation of state of homogeneous nuclear matter and that of the van der Waals.

Since the mid-1980s, many experimental and theoretical works have been devoted to searching for the signals of liquid-gas phase transition in the Fermi energy heavy-ion collisions and relativistic energy projectile fragmentations. The measures used for the studies are the nuclear specific heat capacity (the caloric curves) [8–19], the bimodality in charge asymmetry [20–25], the Fisher droplet model analysis [26–33], the

Landau free energy approach [31,32,34–38], the moment of the charge distributions [28,39–42], the fluctuation properties of the heaviest fragment size (charge) [28,29,42–44], Zipf's law [45,46], the Shannon information entropy [45,47], the multiplicity derivatives proposed for a signature of first-order phase transition [48,49], and the derivative of cluster size [50]. With these measures, much considerable progress has been accomplished on the theoretical as well as on the experimental side for the nuclear liquid-gas phase transition. However, the specific properties of the nuclear liquid-gas phase transition in hot nuclear matter are still under debate and much effort is still required.

In our recent study [51], we have investigated several experimental measures in the framework of the statistical multifragmentation model (SMM) [52–57], focusing on a system with  $A_s = 100$  and  $Z_s/A_s = 0.45$ , to search for suitable observables in heavy-ion collisions and provide a guide for future experiments. In Ref. [51] we demonstrated that a clear signal for the first-order phase transition is observed for the examined measures in a specific system.

In this article we examine the solidarity of the signals for different sizes,  $N/Z$  asymmetries, and volumes of the fragmenting system. We also demonstrate that the charge distributions for different system sizes provide an instructive

\*zhengh@snnu.edu.cn

†liuxingquan@impcas.ac.cn

picture for the signals we observed in SMM events. This article is organized as follows: A brief description of SMM is presented in Sec. II. The results are given in Sec. III. A discussion of system-size effect of SMM is carried out in Sec. IV. A brief summary is given in Sec. V.

## II. STATISTICAL MULTIFRAGMENTATION MODEL

In SMM, the fragmenting system is in the thermal and chemical equilibrium at low density [54–57]. A Markov chain is generated to represent the whole partition ensemble in the version discussed below [55]. All breakup channels (partitions) for nucleons and excited fragments are considered under the conservation of mass, charge, momentum, and energy. The primary fragments are described by liquid drops at a given freezeout volume. Light clusters with mass number  $A \leq 4$  are considered as stable particles (“nuclear gas”). Their masses and spins are taken from the experimental values. Only translational degrees of freedom of these particles are taken into account in the entropy of the system. When the nuclear density becomes very low, the binding energy of clusters is significantly modified by the Pauli blocking and clusterization [58], but these effects are not taken into account in the SMM. Fragments with  $A > 4$  are treated as spherical excited nuclear liquid drops and the free energies  $F_{A,Z}$  are given as a sum of the bulk, surface, Coulomb, and symmetry-energy contributions,

$$F_{A,Z} = F_{A,Z}^B + F_{A,Z}^S + E_{A,Z}^C + F_{A,Z}^{\text{sym}}, \quad (1)$$

where

$$F_{A,Z}^B = (-W_0 - T^2/\varepsilon_0)A, \quad (2)$$

$$F_{A,Z}^S = B_0 A^{2/3} \left[ \frac{T_c^2 - T^2}{T_c^2 + T^2} \right]^{5/4}, \quad (3)$$

$$E_{A,Z}^C = \frac{3e^2}{5r_0} \left[ 1 - (\rho/\rho_0)^{1/3} \right] \frac{Z^2}{A^{1/3}}, \quad (4)$$

$$F_{A,Z}^{\text{sym}} = \gamma(A - 2Z)^2/A - T S_{A,Z}^{\text{sym}}. \quad (5)$$

$W_0 = 16$  MeV is used for the binding energy of infinite nuclear matter, and  $\varepsilon_0 = 16$  MeV is related to the level density;  $B_0 = 18$  MeV is used for the surface coefficient;  $T_c = 18$  MeV is used for the critical temperature of infinite nuclear matter;  $e$  is the charge unit and  $r_0 = 1.17$  fm;  $\rho$  is the density at the breakup and  $\rho_0$  is the normal nuclear density;  $\gamma$  is the symmetry energy parameter; the  $S_{A,Z}^{\text{sym}}$  is the symmetry entropy of fragment introduced in our previous work [57].

The entropy of fragments  $S_{A,Z}$  can be derived from the free energy as

$$S_{A,Z} = -\frac{\partial F_{A,Z}}{\partial T} = S_{A,Z}^B + S_{A,Z}^S + S_{A,Z}^{\text{sym}}. \quad (6)$$

After the primary breakup, the Coulomb acceleration and the secondary de-excitation are performed to get the final secondary fragments. In the de-excitation processes, the Fermi break-up of light primary fragments ( $A < 16$ ), the successive particle emission ( $A > 16$ ), and the fission of heavy nuclei ( $A > 200$ ) are taken into account. SMM is rather successful in describing the multiple production of intermediate mass

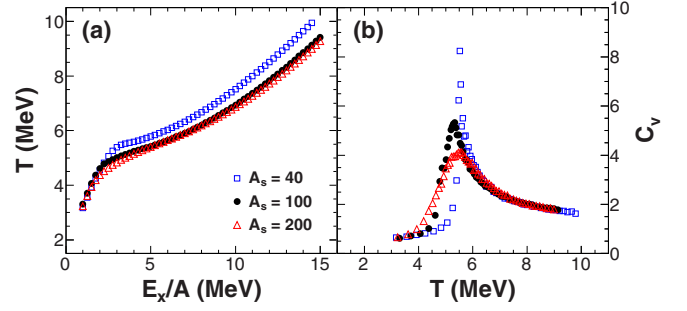


FIG. 1. (a) Caloric curve of fragmenting source of  $A_s = 40$  (open squares),  $A_s = 100$  (solid circles), and  $A_s = 200$  (open triangles) of SMM calculations. (b) The specific heat capacity  $C_v$  extracted from the caloric curve as a function of source temperature. The same charge to mass ratio  $Z_s/A_s = 0.45$  and the same fragmenting volume  $V = 6V_0$  are used.

fragments [59–61] and exhibits a phase transition of the liquid-gas type [62,63].

## III. RESULTS

In our previous work [51], we studied the experimental measures including multiplicity derivatives ( $dM/dT$  and  $dM_{\text{IMF}}/dT$ ), the moment parameters ( $M_2$  and  $\gamma_2$ ), the fluctuation of maximum fragment charge number (NVZ), the Fisher exponent ( $\tau$ ), the bimodal parameter and the Zipf’s law parameter ( $\xi$ ), in the fragmenting system of source mass number  $A_s = 100$ , charge number  $Z_s = 45$ , the fragmenting volume  $V = 6V_0$ , where  $V_0$  is the volume at the normal nuclear density. The default symmetry energy coefficient  $\gamma = 25$  MeV is used. All these measures predict a critical signature at or near to the critical point both for the primary and secondary fragments. Therefore, we will focus on the primary fragments in this study. All the SMM calculations in this section are performed with the same symmetry energy coefficient  $\gamma = 25$  MeV and the same excitation energy range from  $E_x/A = 1$  to 15 MeV with step of 0.25 MeV. More than 1 million events are generated for each  $E_x/A$ .

### A. System-size effect

To investigate the effect of system size on the experimental measures, the SMM calculations are performed with three different source mass numbers,  $A_s = 40, 100,$  and  $200$ , at the same charge to mass ratio,  $Z_s/A_s = 0.45$ , and the same fragmenting volume of  $V = 6V_0$  in this study. The caloric curves and the specific heat capacities are shown in Figs. 1(a) and 1(b), respectively, for system sizes  $A_s = 40$  (open squares),  $A_s = 100$  (solid circles), and  $A_s = 200$  (open triangles). All three systems show a notable plateau of the caloric curve at the excitation energy  $E_x/A \sim 4$  MeV, corresponding to a peak temperature of  $T \sim 5.5$  MeV for  $A_s = 40$ ,  $T \sim 5.3$  MeV for  $A_s = 100$ , and  $T \sim 5.5$  MeV for  $A_s = 200$  at the specific heat capacity,  $C_v$ , as shown in Fig. 1(b). However, the widths of the peak distributions of the specific heat capacity change significantly from  $\sim 0.2$  MeV for  $A_s = 40$  to  $\sim 1$  MeV for  $A_s = 200$ .

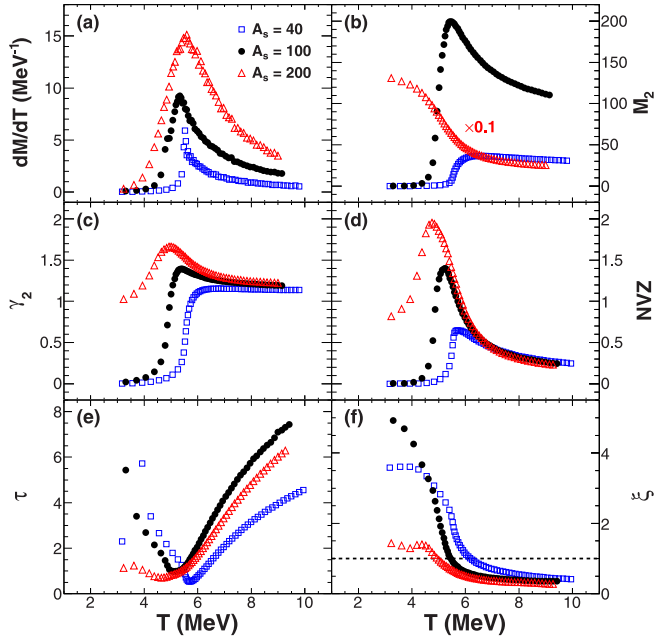


FIG. 2. Extracted values of (a)  $dM/dT$ , (b)  $M_2$ , (c)  $\gamma_2$ , (d)  $NVZ$ , (e)  $\tau$ , and (f)  $\xi$  as a function of source temperature. Open squares, solid circles, and open triangles represent the fragmenting source of  $A_s = 40$ ,  $A_s = 100$ , and  $A_s = 200$ , respectively. The same charge to mass ratio  $Z_s/A_s = 0.45$  and the same fragmenting volume  $V = 6V_0$  are used. A factor of 0.1 is multiplied to  $M_2$  values of system size  $A_s = 200$  for a clear comparison in (b). The horizontal dashed line in (f) shows the critical value of  $\xi = 1$ .

The other experimental measures,  $dM/dT$ ,  $M_2$ ,  $\gamma_2$ ,  $NVZ$ ,  $\tau$ , and  $\xi$ , are also studied for the three system sizes. Figure 2 shows the measures as a function of temperature for (a)  $dM/dT$ , (b)  $M_2$ , (c)  $\gamma_2$ , (d)  $NVZ$ , (e)  $\tau$ , and (f)  $\xi$ , respectively. The  $dM/dT$  has similar behavior as  $C_v$  that the width of peak increases when the system size increases from  $A_s = 40$  to  $A_s = 200$ . The  $M_2$  changes dramatically when the system size increases. In Fig. 2(b) the peak evolves from a shoulder with a sharp rise and small height for  $A_s = 40$  to a clear peak with narrow width for  $A_s = 100$ , and then vanishes for  $A_s = 200$ . The  $\gamma_2$  and  $NVZ$  show similar behavior where a larger signal height is found for a larger system and the phase transition temperature decreases monotonously from  $T \sim 6$  MeV for  $A_s = 40$  to  $T \sim 5$  MeV for  $A_s = 200$  as shown in Figs. 2(c) and 2(d). Similarly to those of  $M_2$ ,  $\gamma_2$  and  $NVZ$ , the phase transition temperature decreases monotonously for the  $\tau$  measure as shown in Fig. 2(e). The Zipf's law parameter ( $\xi$ ) also gives a monotonously decreasing phase transition temperature as shown in Fig. 2(f). The large fluctuation of  $\tau$  and  $\xi$  at low temperature is due to the poor fitting of charge distributions and rank distributions. Most of these measures predict a strong signal of phase transition, but the phase transition temperature depends on the system size except for the caloric curve,  $C_v$ , and  $dM/dT$ . One should note that the system-size effect on nuclear matter phase transition had been studied in several other models [32,64–68]. Some models show different behaviors as that

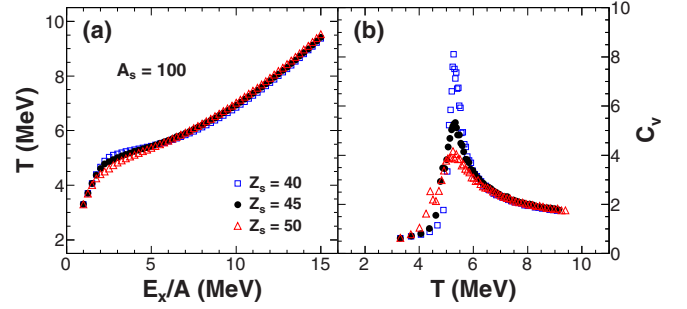


FIG. 3. Similar plots to those in Fig. 1 but with system charge numbers  $Z_s = 40$  (open squares), 45 (solid circles), and 50 (open triangles) at the same system size  $A_s = 100$  and the same fragmenting volume  $V = 6V_0$ .

of SMM. We will further discuss the system-size effect in Sec. IV.

### B. $N/Z$ asymmetry effect

The  $N/Z$  asymmetry of the fragmenting system, which is defined in this work as  $N_s/Z_s = (A_s - Z_s)/Z_s$ , may also affect the critical behavior in fragmenting system. One should note that both the isospin asymmetry and the Coulomb potential change as the  $N/Z$  asymmetry changes. In order to study the  $N/Z$  asymmetry effect, we perform the SMM calculations for three systems with charge number  $Z_s = 40, 45,$  and  $50$  at the same size  $A_s = 100$  and the same fragmenting volume  $V = 6V_0$  for this study. Figure 3(a) shows the caloric curves of these systems and the extracted  $C_v$  are shown in Fig. 3(b). A flatter plateau is observed as  $Z_s$  decreases, which results in a sharper peak in  $C_v$ . The phase transition temperature stays almost same for the three systems.

Figure 4 shows similar plots as those in Fig. 2 but with system charge number  $Z_s = 40$  (open squares), 45 (solid circles), and 50 (open triangles) at the same system size  $A_s = 100$ .  $dM/dT$  shows similar behavior as that of  $C_v$  when charge number of system changes from  $Z_s = 40$  to 50 as shown in Fig. 4(a). All the other five measures give similar decreasing trends of the phase transition temperature when the charge number of system increases from  $Z_s = 40$  to 50 as shown in Figs. 4(b) to 4(f). Similarly to the case for the system-size effect above, these five measures show a monotonic decrease of the phase transition temperature for more neutron poor system, whereas the caloric curve,  $C_v$ , and  $dM/dT$  give a rather solid signal independent of the  $N/Z$  asymmetry of the system.

### C. Fragmenting volume effect

Here we show the effect of fragmenting volume on the experimental measures. The SMM calculations are performed with three different fragmenting volumes,  $V = 4V_0, 6V_0,$  and  $10V_0$ , at the same charge number  $Z_s = 45$  and mass number  $A_s = 100$ . Figure 5 shows the same plots of caloric curves and  $C_v$  as those in Fig. 1, but for different fragmenting volumes. Open squares, solid circles and open triangles represent  $V = 4V_0, 6V_0,$  and  $10V_0$ , respectively. The increasing trend of

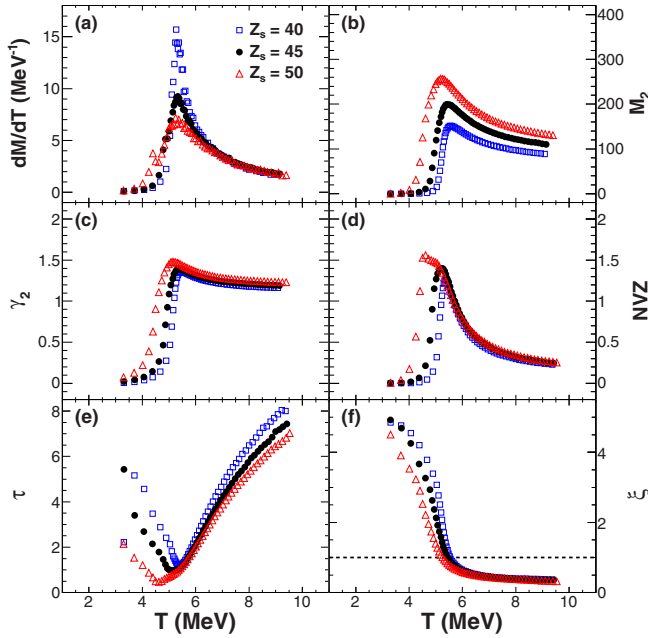


FIG. 4. Similar plots to those in Fig. 2 but with system charge numbers  $Z_s = 40$  (open squares), 45 (solid circles), and 50 (open triangles) at the same system size  $A_s = 100$  and the same fragmenting volume  $V = 6V_0$ .

the phase transition signal width is found for  $C_v$  when the fragmenting volume increases. While all the phase transition temperatures from the different fragmenting volumes are found around  $T = 5.3$  MeV.

Results of the other experimental measures are shown in Fig. 6 in the same style as those in Figs. 2 and 4 but for different fragmenting volumes. Similar shape of  $dM/dT$  and  $C_v$  is also found for different fragmenting volumes as one can see in Fig. 6(a). An increasing signal width (peak or valley) is found for all these experimental measures except for the Zipf's law parameter, which shows difference in the slope. The phase transition temperatures are slightly changes from  $T \sim 5.5$  MeV at  $V = 4V_0$  to  $T \sim 5$  MeV at  $V = 10V_0$  for all these measures, except for NVZ and  $\tau$ , which show a strange peak (valley) at  $T \sim 4$  MeV for  $V = 10V_0$  case. For

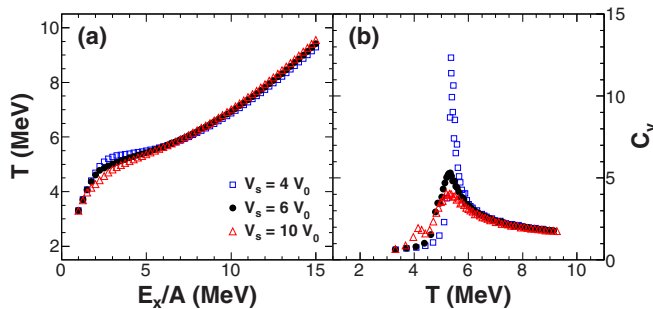


FIG. 5. Similar plots to those in Fig. 1 but for system with fragmenting volumes  $V = 4V_0$  (open squares),  $6V_0$  (solid circles), and  $10V_0$  (open triangles) at the same charge number  $Z_s = 45$  and mass number  $A_s = 100$ .

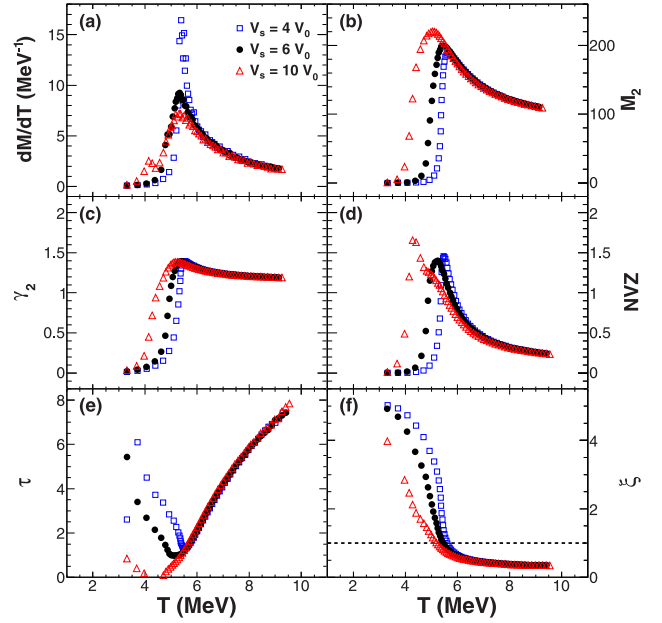


FIG. 6. Similar plots to those in Fig. 2 but for system with fragmenting volumes  $V = 4V_0$  (open squares),  $6V_0$  (solid circles), and  $10V_0$  (open triangles) at the same charge number  $Z_s = 45$  and mass number  $A_s = 100$ .

the system volume effect, we can make a similar conclusion to those of the system size and  $N/Z$  asymmetry.

#### D. Coulomb effect

The Coulomb effect on the phase transition has been observed in many other models [69–72]. In order to study the role of Coulomb force in experimental measures, we perform the SMM calculations without the Coulomb force for fragmenting source of  $A_s = 40, 100,$  and  $200$ , with the same charge to mass ratio  $Z_s/A_s = 0.45$  and the same fragmenting volume  $V = 6V_0$ . Figure 7(a) shows the caloric curves of fragmenting source of  $A_s = 40$  (open circles),  $100$  (open squares)

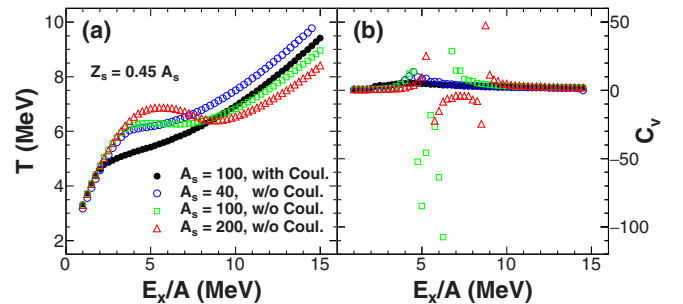


FIG. 7. (a) Caloric curve of fragmenting source of  $A_s = 40$  (open circles),  $A_s = 100$  (open squares), and  $A_s = 200$  (open triangles) without Coulomb force. The solid circles represent the fragmenting source of  $A_s = 100, Z_s = 45$  in SMM calculation with Coulomb force. (b) The specific heat capacity  $C_v$  extracted from caloric curve as a function of source excitation energy. The same fragmenting volume  $V = 6V_0$  is used.

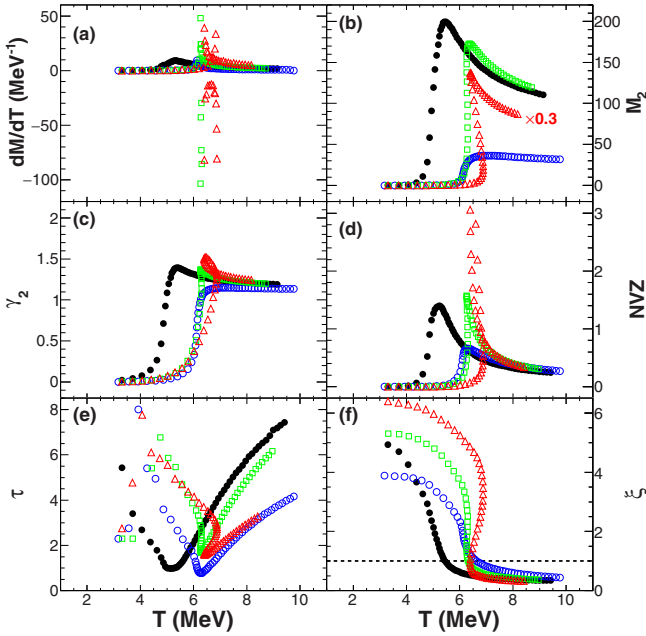


FIG. 8. Similar plots as those in Fig. 2 but for system sizes  $A_s = 40$  (open circles), 100 (open squares), and 200 (open triangles) at the same charge to mass ratio of  $Z_s/A_s = 0.45$  without Coulomb force in the SMM calculations. The solid circles represent the fragmenting source of  $A_s = 100$ ,  $Z_s = 45$  in SMM calculation with Coulomb force for comparison. A factor of 0.3 is multiplied to  $M_2$  of system with  $A_s = 200$  without Coulomb force. The large fluctuation at low temperature in  $\tau$  is due to poor fitting.

squares), and 200 (open triangles) without the Coulomb force as well as that with Coulomb for  $A_s = 100$  (solid circles) for a comparison. For  $A_s = 40$  without Coulomb, a smooth increase of the temperature is observed, similarly to that for  $A_s = 100$  with Coulomb. On the other hand  $A_s = 100$  and 200 without Coulomb show a back-bending in the caloric curves. This back-bending is known as negative heat capacity, which was experimentally reported in the QP data [73,74], and clearly observed in the extracted  $C_v$  plot in Fig. 7(b). However, this negative heat capacity disappears when the Coulomb force is turned ON. This indicates that the Coulomb force strongly suppresses the negative heat capacity, and therefore in nature one cannot observe the negative heat capacity in the multifragmentation process in heavy-ion collisions based on the SMM simulations.

Due to the back bending of caloric curves, the characteristic behavior of the other measures significantly depend on the system size as a function of temperature shown in Fig. 8. The negative  $dM/dT$  is also found at the temperature range from  $T = 6.3$  to 7 MeV for the system size  $A_s = 200$  and at slightly lower temperature around 6.3 MeV for system size  $A_s = 100$ . No negative  $dM/dT$  is found for system size  $A_s = 40$  and the phase transition temperature  $T \sim 6$  MeV is obtained. The other measures give a similar phase transition temperature of  $T \sim 6.3$  MeV as the maximum or minimum behavior for all three systems without the Coulomb force, which is about 1 MeV higher than that of the SMM calculations with Coulomb force. This higher temperature shift is caused by

additional available energy without the Coulomb and also observed in the caloric curve in Fig. 7(a).

### E. The mechanism of phase transition

In the above subsections, we investigate the system size,  $N/Z$  asymmetry and fragmenting volume effects as well as the Coulomb effect on several experimental measures in the framework of SMM. A signal for the first-order phase transition for all the measures is observed. The signal is rather solid for the caloric curve,  $C_v$ , and  $dM/dT$ , whereas for the other five measures the phase transition temperature decreases monotonically for a larger size, more proton rich, and larger volumes of the systems for most of the cases, and the characteristic shape of the signal for a given measure changes in a similar fashion as a function of the size or proton richness or volume of the system. A negative heat capacity is observed for systems with  $A_s \geq 100$  without the Coulomb force, but it disappears with the Coulomb. In this subsection, we further discuss the mechanism of liquid-gas phase transition through the evolution of charge distributions.

The charge distribution of fragments is compared for a given  $E_x/A$  value in every 2 MeV for three system sizes,  $A_s = 40$  (solid histogram), 100 (dashed histogram), and 200 (dotted histogram) for SMM calculations with Coulomb (left) and without Coulomb (right) at the same charge to mass ratio  $Z_s/A_s = 0.45$  and the same fragmenting volume  $V = 6V_0$  in Fig. 9. At  $E_x/A = 2$  MeV, all distributions show a similar structure except for  $A_s = 200$  with Coulomb, see Figs. 9(a) and 9(f). The distributions consist of two components, one is large fragments with  $Z \sim Z_s$  and the other is dominated by  $Z = 1$  and 2 particles. This indicates that these events mainly consist of a large fragment and light particles. It resembles the particle distribution from evaporation decays. We label the process “evaporation mode” and it is in a liquid state, which is represented by the existence of a large fragment. For  $A_s = 200$  with Coulomb, the distribution is quite different from the others at the same excitation energy. There is a large bump around  $Z \sim Z_s/2$ . This component is from fission decay, which is caused by a large Coulomb energy. When the Coulomb is turned off, this fission decay channel is closed and the distribution becomes very similar to those of  $A_s = 40$  and 100 with Coulomb. When  $E_x/A \geq 8$  MeV, smaller IMFs become dominant for all cases. These IMFs are produced through a multifragmentation decay and they are in a gaslike state, which is labeled “multifragmentation mode”.

A clear evolution of the two modes in the charge distribution, an evaporation mode, or fission mode at the lower excitation energy to the multifragmentation mode at the higher excitation energy is observed. This provides an instructive picture of the observed plateau in the caloric curves, which reflects a transition of liquid-gas type in SMM.

A significant difference on the Coulomb force for a large system was predicted in the multicanonical system in Ref. [70]. In the SMM model, the absence of the Coulomb force generates the negative heat capacity as the transition from the evaporation mode to the multifragmentation mode. When the Coulomb is turned on, the evaporation mode is replaced by the fission mode and the negative heat capacity

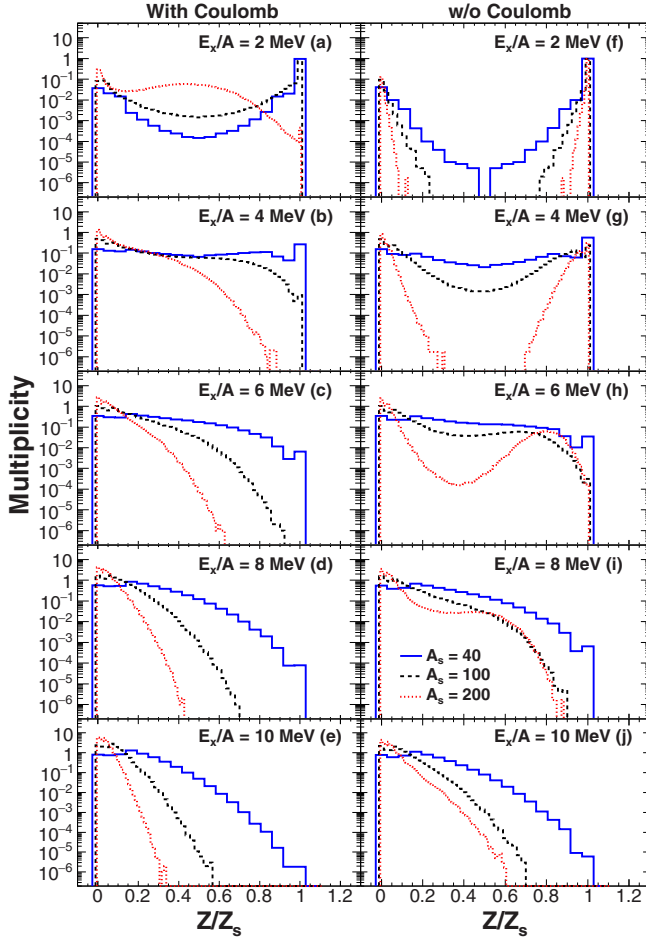


FIG. 9. Charge distributions of system sizes  $A_s = 40$  (solid histogram), 100 (dashed histogram), and 200 (dotted histogram) for excitation energy from  $E_x/A = 2$  to 10 MeV in 2 MeV step for the SMM calculations with Coulomb (left) and without Coulomb (right) at the same charge to mass ratio  $Z_s/A_s = 0.45$  and the same fragmenting volume  $V = 6V_0$ .

disappears. No drastic change is observed in the lighter system for the existence (absence) of the Coulomb force, except for the phase transition temperature values, which increase 1–2 MeV for the absence of the Coulomb force. For the lighter system, the transition from the evaporation mode to the multifragmentation mode occurs with or without Coulomb with the increase of the excitation energy.

#### IV. DISCUSSION

In Sec. III A, the specific heat capacity  $C_v$ ,  $dM/dT$  as well as Fisher exponent  $\tau$  predict a very similar phase transition temperature  $T \sim 5.5$  MeV for three different system sizes. The signal width increases as the system size increases for these measures. These observables are quite different from the results of a percolation model or a lattice gas model, in which the phase transition signatures become prominent when the system size increases [64,66,75,76]. In order to address the different system-size effects of SMM and these models, the antisymmetrized molecular dynamics (AMD)

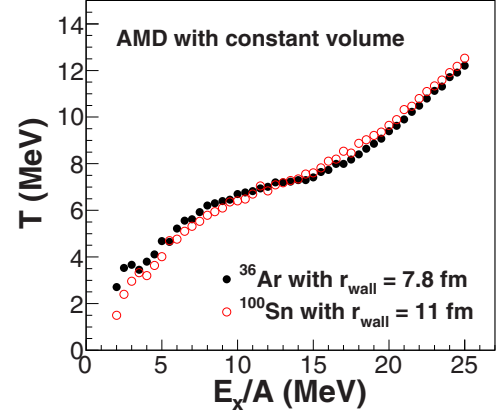


FIG. 10. Caloric curves of  $^{36}\text{Ar}$  at  $r_{\text{wall}} = 7.8$  fm (solid circles) and  $^{100}\text{Sn}$  at  $r_{\text{wall}} = 11$  fm (open circles) from AMD.

model [17,18,77–79] is adopted. In those studies [17,18], a static nature of the hot nuclear matter is studied, confining hot nucleons in a fixed volume. A back-bending is observed in the caloric curve along a constant pressure as a signature of the phase transition for a rather small system of  $A = 36$ . In our study, however, we focus on the critical behavior at a constant volume, just because it is built in SMM. In this study we apply the model for  $^{36}\text{Ar}$  and  $^{100}\text{Sn}$  systems at a constant volume with  $r_{\text{wall}} = 7.8$  and 11 fm, respectively, which give the same average density of  $\rho = 0.018 \text{ fm}^{-3}$ .  $r_{\text{wall}}$  is the radius of the potential wall used for the confinement of the nucleons. The density corresponds to  $V \sim 9V_0$  in SMM simulations, but as discussed in Sec. III C, no significant change on the phase transition is observed in SMM. The time evolution of AMD is calculated up to 99 000 fm/c for  $^{36}\text{Ar}$  and 25 000 fm/c for  $^{100}\text{Sn}$ . The other procedures are the same as those in Ref. [17].

Figure 10 shows the resultant caloric curves of  $^{36}\text{Ar}$  (solid circles) and  $^{100}\text{Sn}$  (open circles) from AMD. One can see that the flat plateaus are observed at temperature  $T \sim 7$  MeV for both  $^{36}\text{Ar}$  and  $^{100}\text{Sn}$ , which reflects a similar phase transition temperature for the two different system sizes in the AMD simulations. A flatter plateau is found for the lighter system of  $^{36}\text{Ar}$ , which indicates a narrower peak in the specific heat capacity  $C_v$ . Therefore, the AMD results of the system-size effect are consistent to those from the SMM calculations. This suggests that the phase transition in SMM reflects the nucleon-nucleon interaction effect through the binding energy, which is not taken into account in the percolation or the lattice gas model. The AMD results support the SMM results, which is based on a thermodynamic concept, and the nucleon-nucleon interaction through the binding energy plays a crucial role for the phase transition signatures discussed in Sec. III.

#### V. SUMMARY

We investigate the system size,  $N/Z$  asymmetry, and fragmenting volume effects as well as the Coulomb effect on several experimental measures including caloric curve,  $C_v$ ,  $dM/dT$ ,  $M_2$ ,  $\gamma_2$ ,  $NVZ$ ,  $\tau$ , and  $\xi$ , which provide

signatures for nuclear liquid-gas phase transition in heavy-ion collisions in the framework of SMM.

The caloric curve,  $C_v$ , and  $dM/dT$  give a solid signal for the first-order phase transition, independent of the system sizes, the  $N/Z$  asymmetries, and the volumes of the system at a similar value of the phase transition temperature, though the shape of the signal slightly depends on the conditions as a function of the  $E_x/A$ . For the other five measures,  $M_2$ ,  $\gamma_2$ ,  $NVZ$ ,  $\tau$ , and  $\xi$ , all give a phase transition signal, but the phase transition temperature decreases monotonically, as the size or proton richness or volume of the system increases. Since the caloric curve,  $C_v$ , and  $dM/dT$  show a consistent behavior at or near the phase transition temperature, they provide the best solid measure for the first-order phase transition.

A negative heat capacity is observed for system size  $A_s \geq 100$  without the Coulomb force. The calculations do not show negative heat capacity when Coulomb force is on even for system size greater than 200. This is because the Coulomb force strongly enhances the fission decay at a low excitation energy,

and the negative heat capacity, which is from the transition from the evaporation mode to the multifragmentation mode, disappears.

## ACKNOWLEDGMENTS

The authors thank A. S. Botvina for providing his code and many fruitful discussions. The authors also thank A. Ono for providing his code. This work is supported by the National Natural Science Foundation of China (Grants No. 11805138 and No. 11705242), the Program for the CAS ‘‘Light of West China’’ (Grant No. 29Y601030), the National MCF Energy R&D Program (Grant No. MOST 2018YFE0310200), and the Fundamental Research Funds For the Central Universities (Grants No. YJ201820 and No. GK201903022). This work is also supported by the US Department of Energy under Grant No. DE-FG02-93ER40773 and the Robert A. Welch Foundation under Grant No. A330.

- 
- [1] N. Bohr, *Nature* **137**, 344 (1936).
- [2] B. Borderie and M. F. Rivet, *Prog. Part. Nucl. Phys.* **61**, 551 (2008).
- [3] F. Gulminelli, W. Trautmann, S. J. Yennello, and Ph. Chomaz, *Eur. Phys. J. A* **30**, 1 (2006); and related topics in the volume.
- [4] Ph. Chomaz, M. Colonna, and J. Randrup, *Phys. Rep.* **389**, 263 (2004).
- [5] J. E. Finn, S. Agarwal, A. Bujak *et al.*, *Phys. Rev. Lett.* **49**, 1321 (1982).
- [6] R. W. Minich, S. Agarwal, A. Bujak *et al.*, *Phys. Lett. B* **118**, 458 (1982).
- [7] A. S. Hirsch, A. Bujak, E. Finn *et al.*, *Nucl. Phys. A* **418**, 267 (1984).
- [8] E. Suraud, C. Grégoire, and B. Tamain, *Prog. Part. Nucl. Phys.* **23**, 357 (1989); and references therein.
- [9] D. H. E. Gross, *Prog. Part. Nucl. Phys.* **30**, 155 (1993); and references therein.
- [10] K. Hagel, D. Fabris, P. Gonthier *et al.*, *Nucl. Phys. A* **486**, 429 (1988).
- [11] R. Wada, D. Fabris, K. Hagel *et al.*, *Phys. Rev. C* **39**, 497 (1989).
- [12] D. Cussol, G. Bizard, R. Brou *et al.*, *Nucl. Phys. A* **561**, 298 (1993).
- [13] J. Pochodzalla, T. Möhlenkamp, T. Rubehn *et al.*, *Phys. Rev. Lett.* **75**, 1040 (1995).
- [14] R. Wada, R. Tezkratt, K. Hagel *et al.*, *Phys. Rev. C* **55**, 227 (1997).
- [15] K. Hagel, R. Wada, J. Cibor *et al.*, *Phys. Rev. C* **62**, 034607 (2000).
- [16] J. B. Natowitz, R. Wada, K. Hagel *et al.*, *Phys. Rev. C* **65**, 034618 (2002).
- [17] T. Furuta and A. Ono, *Phys. Rev. C* **74**, 014612 (2006).
- [18] T. Furuta and A. Ono, *Phys. Rev. C* **79**, 014608 (2009).
- [19] S. Das Gupta, A. Z. Mekjian, and M. B. Tsang, Liquid-Gas Phase Transition in Nuclear Multifragmentation, in *Advances in Nuclear Physics*, edited by J. W. Negele and E. W. Vogt, *Advances in the Physics of Particles and Nuclei* Vol. 26 (Springer, Boston, MA, 2001), pp. 89–166.
- [20] O. Lopez, D. Lacroix, and E. Vient, *Phys. Rev. Lett.* **95**, 242701 (2005).
- [21] M. Pichon, B. Tamain, R. Bougault *et al.* (INDRA and ALADIN Collaborations), *Nucl. Phys. A* **779**, 267 (2006).
- [22] A. Le Fèvre and J. Aichelin, *Phys. Rev. Lett.* **100**, 042701 (2008).
- [23] A. Le Fèvre, J. Aichelin, C. Hartnack *et al.* (INDRA and ALADIN Collaborations), *Phys. Rev. C* **80**, 044615 (2009).
- [24] E. Bonnet, D. Mercier, B. Borderie *et al.* (INDRA and ALADIN Collaborations), *Phys. Rev. Lett.* **103**, 072701 (2009).
- [25] B. Borderie, E. Bonnet, F. Gulminelli *et al.* (INDRA and ALADIN Collaborations), *Nucl. Phys. A* **834**, 535c (2010).
- [26] M. E. Fisher, *Rep. Prog. Phys.* **30**, 615 (1969); *Physics* **3**, 255 (1967).
- [27] J. B. Elliott, L. G. Moretto, L. Phair *et al.*, *Phys. Rev. Lett.* **88**, 042701 (2002).
- [28] Y. G. Ma, J. B. Natowitz, R. Wada *et al.*, *Phys. Rev. C* **71**, 054606 (2005).
- [29] Y. G. Ma, J. B. Natowitz, R. Wada *et al.*, *Nucl. Phys. A* **749**, 106c (2005).
- [30] Y. G. Ma, R. Wada, K. Hagel *et al.*, *Phys. Rev. C* **69**, 031604(R) (2004).
- [31] M. Huang, R. Wada, Z. Chen *et al.*, *Phys. Rev. C* **82**, 054602 (2010).
- [32] G. Giuliani, H. Zheng, and A. Bonasera, *Prog. Part. Nucl. Phys.* **76**, 116 (2014).
- [33] W. Lin, X. Liu, M. R. D. Rodrigues *et al.*, *Phys. Rev. C* **90**, 044603 (2014).
- [34] A. Bonasera, Z. Chen, R. Wada *et al.*, *Phys. Rev. Lett.* **101**, 122702 (2008).
- [35] R. Tripathi, A. Bonasera, S. Wuenschel *et al.*, *Phys. Rev. C* **83**, 054609 (2011).
- [36] R. Tripathi, A. Bonasera, S. Wuenschel *et al.*, *J. Phys.: Conf. Ser.* **312**, 082043 (2011).
- [37] R. Tripathi, A. Bonasera, S. Wuenschel *et al.*, *Int. J. Mod. Phys. E* **21**, 1250019 (2012).

- [38] J. Mabilia, A. Bonasera, H. Zheng *et al.*, *Phys. Rev. C* **87**, 017603 (2013).
- [39] X. Campi, *Phys. Lett. B* **208**, 351 (1988).
- [40] X. Campi, *J. Phys. A* **19**, L917 (1986).
- [41] S. Das Gupta, A. Z. Mekjian, *Phys. Rev. C* **57**, 1361 (1998).
- [42] P. F. Mastinu, M. Belkacem, F. Gramegna, and P. M. Milazzo, *Phys. Rev. C* **57**, 831 (1998).
- [43] R. Botet, M. Ploszajczak, A. Chbihi, B. Borderie, D. Durand, and J. Frankland, *Phys. Rev. Lett.* **86**, 3514 (2001).
- [44] J. D. Frankland, A. Chbihi, A. Mignon *et al.* (INDRA and ALADIN Collaborations), *Phys. Rev. C* **71**, 034607 (2005).
- [45] Y. G. Ma, *Phys. Rev. Lett.* **83**, 3617 (1999).
- [46] Y. G. Ma, *Eur. Phys. J. A* **6**, 367 (1999).
- [47] C. W. Ma and Y. G. Ma, *Prog. Part. Nucl. Phys.* **99**, 120 (2018).
- [48] S. Mallik, G. Chaudhuri, P. Das, and S. Das Gupta, *Phys. Rev. C* **95**, 061601(R) (2017).
- [49] S. Das Gupta, S. Mallik, and G. Chaudhuri, *Phys. Rev. C* **97**, 044605 (2018).
- [50] P. Das, S. Mallik, and G. Chaudhuri, *Phys. Lett. B* **763**, 364 (2018).
- [51] W. Lin, P. Ren, H. Zheng, X. Liu, M. Huang, R. Wada, and G. Qu, *Phys. Rev. C* **97**, 054615 (2018).
- [52] X. Z. Zhang, D. H. E. Gross, S. Y. Xu, and Y. M. Zheng, *Nucl. Phys. A* **461**, 641 (1987).
- [53] X. Z. Zhang, D. H. E. Gross, S. Y. Xu, and Y. M. Zheng, *Nucl. Phys. A* **461**, 668 (1987).
- [54] J. P. Bondorf, A. S. Botvina, A. S. Iljinov, I. N. Mishustin, and K. Sneppen, *Phys. Rep.* **257**, 133 (1995).
- [55] A. S. Botvina and I. N. Mishustin, *Phys. Rev. C* **63**, 061601(R) (2001).
- [56] G. A. Souliotis, A. S. Botvina, D. V. Shetty, A. L. Keksis, M. Jandel, M. Veselsky, and S. J. Yennello, *Phys. Rev. C* **75**, 011601(R) (2007).
- [57] W. Lin, H. Zheng, P. Ren *et al.*, *Phys. Rev. C* **97**, 044603 (2018).
- [58] S. Typel, G. Röpke, T. Klähn, D. Blaschke, and H. H. Wolter, *Phys. Rev. C* **81**, 015803 (2010).
- [59] A. S. Botvina, I. N. Mishustin, M. Begemann-Blaich *et al.*, *Nucl. Phys. A* **584**, 737 (1995).
- [60] M. D'Agostino, A. S. Botvina, P. M. Milazzo *et al.*, *Phys. Lett. B* **371**, 175 (1996).
- [61] M. D'Agostino, A. S. Botvina, M. Bruno *et al.*, *Nucl. Phys. A* **650**, 329 (1999).
- [62] N. Buyukcizmeci, R. Ogul, and A. S. Botvina, *Eur. Phys. J. A* **25**, 57 (2005).
- [63] R. Ogul, N. Buyukcizmeci, and A. S. Botvina, *Nucl. Phys. A* **749**, 126c (2005).
- [64] J. B. Elliott, M. L. Gilkes, J. A. Hauger *et al.*, *Phys. Rev. C* **49**, 3185 (1994).
- [65] A. Bonasera, M. Bruno, C. O. Dorso, and P. F. Mastinu, *La Riv. Nuovo Cimento* **23**, 2 (2000).
- [66] T. Li, W. Bauer, D. Craig *et al.*, *Phys. Rev. C* **49**, 1630 (1994).
- [67] W. Bauer, *Phys. Rev. C* **38**, 1297 (1988).
- [68] S. Mallik, F. Gulminelli, and G. Chaudhuri, *Phys. Rev. C* **92**, 064605 (2015).
- [69] C. B. Das, S. Das Gupta, W. G. Lynch, A. Z. Mekjian, and M. B. Tsang, *Phys. Rep.* **406**, 1 (2005).
- [70] F. Gulminelli, Ph. Chomaz, A. H. Raduta, and A. R. Raduta, *Phys. Rev. Lett.* **91**, 202701 (2003).
- [71] M. J. Ison and C. O. Dorso, *Phys. Rev. C* **69**, 027001 (2004).
- [72] G. Chaudhuri, S. Das Gupta, and F. Gulminelli, *Nucl. Phys. A* **815**, 89 (2009).
- [73] M. D'Agostino, F. Gulminelli, Ph. Chomaz *et al.*, *Phys. Lett. B* **473**, 219 (2000).
- [74] M. D'Agostino, R. Bougault, F. Gulminelli *et al.*, *Nucl. Phys. A* **699**, 795 (2002).
- [75] L. G. Moretto, K. A. Bugaev, J. B. Elliott, R. Ghetti, J. Helgeson, and L. Phair, *Phys. Rev. Lett.* **94**, 202701 (2005).
- [76] J. B. Elliott, M. L. Gilkes, J. A. Hauger *et al.*, *Phys. Rev. C* **55**, 1319 (1997).
- [77] A. Ono, H. Horiuchi, T. Maruyama, and A. Ohnishi, *Phys. Rev. Lett.* **68**, 2898 (1992).
- [78] A. Ono, H. Horiuchi, T. Maruyama, and A. Ohnishi, *Prog. Theor. Phys.* **87**, 1185 (1992).
- [79] A. Ono and H. Horiuchi, *Prog. Part. Nucl. Phys.* **53**, 501 (2004).